Check for updates

A DFT exploration of the optoelectronic and thermoelectric features of a novel halide double perovskite A$_2$YAuI$_6$ (A = Rb, Cs) for solar cell and renewable energy applications

Abrar Nazir,[a] Aparna Dixit,[b] Ejaz Ahmad Khera, [ID] *[a] Mumtaz Manzoor,[c] Ramesh Sharma [ID] [d] and A. J. A. Moayad*[e]

Double-perovskite halides are potentially useful materials for producing renewable energy and are thought to meet the necessary criteria for addressing energy scarcity issues. Consequently, investigations into these halides have potential uses in the fields of thermoelectric and solar cell gadgets. The physical properties of A$_2$YAuI$_6$ (A = Rb, Cs) double perovskite halides were also investigated in the current work using DFT calculations based on the FP-LAPW approach for applications in renewable energy devices. The calculated Goldschmidt's tolerance factor and formation energy demonstrate that the explored halides are structurally and thermodynamically stable in the cubic phase. By analyzing mechanical properties, the measured Pugh and Poisson ratios demonstrate a ductile nature. In addition, we used electrical characteristics to compute bandgaps both with and without spin orbit coupling (SOC). We calculated the bandgap values of Rb$_2$YAuI$_6$ (E_g = 1.73 eV) and Cs$_2$YAuI$_6$ (E_g = 1.70 eV) using modified Becke–Johnson with spin orbit coupling (mBJ + SOC) potentials in order to get corrected bandgap values with respect to experimental data. Additionally, the optical characteristics of the halides under study were analyzed in light of their complex dielectric functions. Our computed optical parameter results clearly show that these halides have the best light absorption in the UV-visible region, indicating their suitability for use in solar cell applications. The power factor (PF), thermal conductivity, figure of merit, electrical conductivity, and Seebeck coefficient were computed to analyze transport characteristics against chemical potential, carrier concentration and temperature. Our findings can prove beneficial for further experimental research aimed at assessing A$_2$YAuI$_6$ (A = Rb, Cs) in relation to applications using renewable energy devices.

1. Introduction

The demand for alternatives to fossil fuels has dramatically increased as a result of the shortage of traditional energy sources. The techniques that researchers are developing can draw energy from renewable resources. One of the primary sources of energy from renewable sources is the sun. Researchers can turn the heat and light energy from the sun into electrical energy using solar cells and thermoelectric generators. However, recent studies have shown that lead-involved hybrid perovskites can be created by mixing organic and inorganic components. Amongst the different material types, perovskites are one of the most popular materials that have been extensively explored for thermoelectric and photovoltaic applications, particularly in the field of perovskite solar cells. Perovskites are well-known for their cost-effectiveness, high absorption coefficient, adjustable bandgap, low effective mass, free availability, and stability in their structure. Moreover, they are simple to synthesize and low in weight.[1–10] However, because of their low stability and toxicity, as seen in CH$_3$NH$_3$PbX$_3$ (where X = Cl, Br and I) perovskites, they are hazardous to the environment and are of little utility in the solar cell system.[1–3] Lead-free material manufacturing is therefore urgently needed. Using lead-free products can help to protect the environment as well as reduce the need for fossil fuels. Consequently, lead-free double perovskites have drawn much interest from the scientific community.

[a] *Department of Physics Bahawalnagar Campus, The Islamia University of Bahawalpur, Bahawalpur, 63100, Pakistan. E-mail: ejaz.khera@iub.edu.pk*

[b] *Department of Basic Sciences and Humanities, Pranveer Singh Institute of Technology, Kanpur, U. P, India*

[c] *Institute of Physics, Slovak Academy of Sciences, 84511 Bratislava, Slovakia*

[d] *Department of Applied Science, Feroze Gandhi Institute of Engineering and Technology, Raebareli-229001, Uttar Pradesh, India. E-mail: sharmadft@gmail.com*

[e] *Department of Materials Science, Malawi University of Science and Technology, P. O Box 5196, Limbe, Malawi. E-mail: mailme_moya123@rediffmail.com*

Among the subclasses of perovskite structure, double perovskites has properties that combine the chemical and physical characteristics, whereas we cannot see these properties in a simple perovskite structure. These materials come in a greater variety of metals and oxidation states. This diversity makes it possible to enhance the optoelectronic characteristics that are beneficial for solar energy technologies. Shi et al.[11] created lead-free double perovskites that relax ferroelectrics in order to investigate the piezoelectric behavior. These rare-earth perovskites have great qualities that make them appropriate for solar energy applications. Still, a large number of researchers substituted tin-based halide perovskites for lead-based perovskites, specifically $CH_3NH_3PbX_3$.[12–14] Researchers are searching for various perovskites that could be used as solar absorber materials because of the breakdown and instability of these perovskites.[15–17] Lead-free double perovskite Cs_2AgBiX_6 has been the subject of recent investigations, and considered as an environmentally friendly substitute for $CH_3NH_3PbI_3$.[18] Wang et al. have proposed the use of double perovskite $Cs_2AgBiBr_6$ in conjunction with reduced graphene oxide to produce photocatalytic hydrogen.[19] The optical, thermoelectric, magnetic and electronic characteristics of the $Ca_2Cr_{1-x}Ni_xOsO_6$ double perovskites were observed by Bhandari et al.[20] using density functional theory. The results demonstrated that the double perovskite that was produced had a bandgap of around (0.6 eV), and was optically isotropic and ferromagnetic. The fact that compounds with narrow bandgaps, such as PbTe and Bi_2Te_3,[21] are thought to be appropriate for thermoelectric generators is highly interesting. According to a study carried out by Haque et al.,[22] $Cs_2InAgCl_6$ has a direct band gap of 3.3 eV with a ZT value of 0.94 that makes it appropriate for thermoelectric appliances.

The optoelectronic and thermoelectric features of Cs_2ScAgY_6 (Y = Cl, Br and I) have been studied by Khan et al.[23] These compounds have demonstrated indirect bandgap values of 1.55 eV and 1.9 eV at 300 K, as well as a figure of merit value of 0.74. X_2ScInI_6 (X = Rb, Cs) was examined using DFT by Noor et al.,[24] and they were shown to be useful for optoelectronic devices. Iqbal et al. previously studied the opto-electronic and transport characteristics of Rb_2AlInX_6 (X = Cl, Br, I).[25] By applying first-principle computations, Anbarasan et al.[26] reported the mechanical, structural, and opto-electronic features of Cs_2AgInY_6 (Y = Cl, Br and I). Nazir et al.[27] has examined the double perovskite $X_2LiInBr_6$ (X = Rb, Cs) for solar cell applications. Due to their absorption and optical conductivity in the visible region of the electromagnetic spectrum, they are suitable candidates for solar cell applications.

In the present study, we have computed the structural, electronic, optical, and thermoelectric properties of novel double perovskite A_2YAuI_6 (A = Rb, Cs) compounds. As per our knowledge, neither experimental nor theoretical study has been performed earlier for these compounds. Our results would hopefully be helpful for future experimental and theoretical research studies in evaluating the A_2YAuI_6 (A = Rb, Cs) double perovskite for applications related to energy harvesting technologies.

2. Methodology

In our study, we used FP-LAPW[28,29] method-based WIEN2k code[28] to compute the optoelectronic and transport characteristics of Rb_2YAuI_6 and Cs_2YAuI_6 via DFT calculations. Using Murnaghan equations of states for the examined compounds, the PBE-GGA functional was utilized to precisely calculate the lattice constants, ground state energy, and bulk modulus.[30–32] Although it facilitates the computation of structural parameters, this approximation underestimates electronic parameters, particularly the band gap. Despite having comparable accuracy, the TB-mBJ[33] potential is more flexible and requires less computation time than the PBE-GGA.[34] Therefore, the TB-mBJ potential is applied over PBE-GGA in order to accurately measure the band gap. Additionally, since the SOC coupling influences the band gap materials of heavy elements, it has also been included. While the electronic system solution is plane wave-like in the interstitial area, it is believed to be spherically harmonic within the muffin-tin sphere. The structure is continuously optimized until the strain-force for every atom is zero. The starting parameters have been adjusted by setting the angular momentum $\ell_{max} = 10$ in the reciprocal lattice, Gaussian parameter $G_{max} = 14$, and the product of the wave vector and muffin radius $K_{max} \times R_{MT} = 8$. When the energy released from the system becomes constant, the 2000 k-point is used to select the k-mesh of the order of $12 \times 12 \times 12$.[35] The optical properties were calculated by employing Kramers–Kronig equations. This is thought to be the convergence criterion's threshold limit in terms of the precision of the results acquired. The charge convergence is taken into account at 0.01 mRy. For the separation of the core and valence states, the cut-off energy was selected as −9 Ry. The core state is explained by the lower energy range compared to those equipped states. The thermoelectric parameters, such as the Seebeck coefficient, electrical conductivity, thermal conductivity, figure of merit (ZT) and power factor, were calculated in the temperature range of 100–1200 K against chemical potential and carrier concentration. The Boltztrap code,[36] which is based on the classical Boltzmann transport theory, was used to calculate the transport features by utilizing the optimized electrical structures via Tb-mBJ and the convergent energy. For the thermoelectric characteristics calculation, a fine grid mesh has been utilized ($44 \times 44 \times 44$).

3. Structural and mechanical properties

For all computations, we used the crystal structures of the Rb_2YAuI_6 and Cs_2YAuI_6 compounds with the space group of $Fm\bar{3}m$ #225. The crystal structure of A_2YAuI_6 (A = Rb, Cs) is presented in Fig. 1. Using the Murnaghan equation[37] of states, we optimized both compounds using PBE-GGA to obtain the ground state lattice parameters.

$$E_{tot}(V) = E_o(V) + \frac{B_oV}{B'(B'-1)}\left[B\left(1 - \frac{V_o}{V}\right) + \left(\frac{V_o}{V}\right)^{B'} - 1\right] \quad (1)$$
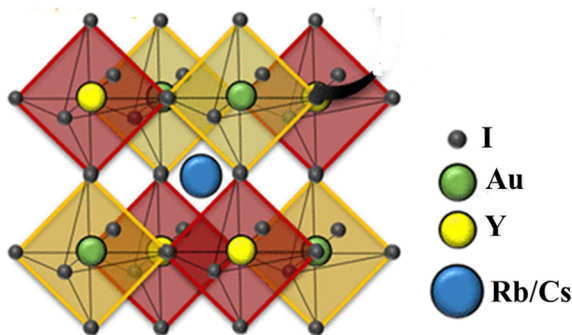
Fig. 1 Crystal structure of A_2YAuI_6 (A = Rb, Cs).

Fig. 2 Energy *versus* volume optimization curves of A_2YAuI_6 (A = Rb, Cs).

The bulk modulus and ground state lattice constant (a_0) are determined *via* the volume optimization method, as depicted in Table 1. The ground state energy *versus* optimized volume graphs of studied compounds are shown in Fig. 2. The determined values of a_0 increase from Rb_2YAuI_6 to Cs_2YAuI_6, as shown in Table 1, because the atomic radii increase from 2.48 Å (Rb) to 2.65 Å (Cs). The increase in cationic size leads to a decrease in the density (and therefore the solidity of the materials), which is why the bulk modulus B_0 (20.33 GPa 19.87 GPa) drops when Rb replaces Cs. Applying the formula,[38] we determine Goldschmidt's tolerance factor (t_G) for the computation of structural stability.

$$t_G = (r_{Rb/Cs} + r_I)/\sqrt{2}(r_{Y,Au} + r_I) \quad (2)$$

here, $r_{Rb/Cs}$, r_Y, r_{Au} and r_I are the atomic radius of Rb/Cs, Y, Au and I atoms, respectively. Goldschmidt's criterion typically reaches unity for stable cubic perovskites in an ideal scenario. Because of this, the range of values between 0.8 and 1.4 is significant for stable cubic structures. Table 2 shows our computed values in the above range. As a result, the compounds under study are stable in their cubic state. A comparative investigation demonstrated that Cs_2YAuI_6 is closer to the ideal limit than Rb_2YAuI_6. Additionally, the compound's thermodynamic stability is demonstrated by the chemical equation which computes the formation energy as follows:

$$\Delta H_f = E_{Total}(Rb/Cs_aY_bAu_cI_d) - aE_{Rb/Cs} - bE_Y - cE_{Au} - dE_I \quad (3)$$

where $E_{Rb/Cs}$, E_Y, E_{Au}, and E_I denote the energies for the isolated Rb/Cs, Y, Au, and I atoms, respectively, and $E_{Total}(Rb/Cs_aY_bAu_cI_d)$ reflects the entire sum of energy of the examined compounds. In the equation above, the numbers a, b, c, and d represent the
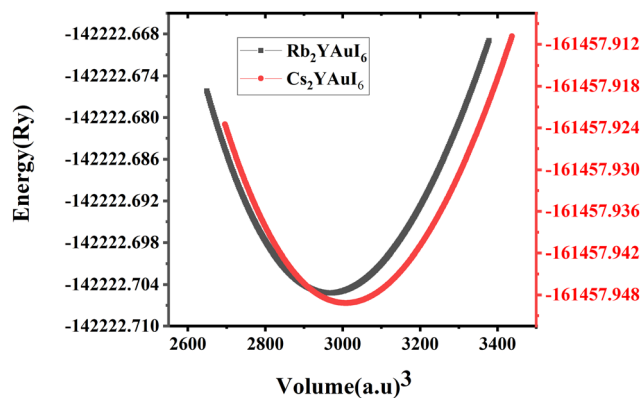
number of corresponding atoms. The quantity of energy lost during the process of material production is primarily represented by the negative value of ΔH_f. In actuality, it is essential to the material's stability. As a result, the calculated values shown in Table 1 validate the synthesized compounds thermodynamic stability.[39] It is evident from the data once more that Cs_2YAuI_6 is more stable than Rb_2YAuI_6.

The compounds are classified as ductile ($B/G > 1.75$) and brittle ($B/G < 1.75$) based on the critical limit of 1.75 of Pugh's ratio (B/G). The ductile criterion for the materials is defined by the Poisson ratio (v), which is defined as σ greater than 0.26.[40] It has been demonstrated that Cs_2YAuI_6 is more ductile than Rb_2YAuI_6 due to its greater B/G and v values. Using the Navier equation of states, we can also compute the sound velocity as the mean of the transverse and longitudinal components of the velocities.[41,42] However, Rb_2YAuI_6 has a greater value than Cs_2YAuI_6. This directly affects the Debye temperature, which is determined using the following formula:

$$\Theta_D = \frac{h}{k_B}\left[\frac{3n}{4\pi}\frac{N_A\rho}{M}\right]^{1/3}v_m \quad (4)$$

where ρ denotes material density, M denotes molecular mass, v_m stands for average sound velocity, N_A stands for Avogadro number, and k_B represents the Boltzmann constant. Table 1 displays the computed value of the Debye temperature, which is greater for Rb_2YAuI_6 than Cs_2YAuI_6. The specific heat capacity is directly impacted by the Debye temperature. The calculated results clearly show that Rb_2YAuI_6 has a greater capacity to withstand the heat produced by the lattice vibration.[38,43] Moreover, the compounds' thermodynamic stability is dependent on an increasing temperature.

Table 1 Calculated lattice parameter a (Å), bulk modulus B, its derivative B_P, the minimum total energy E_{tot}, energy of cohesion E_{coh}, of A_2YAuI_6 (A = Rb, Cs)

XC	a (Å)	V (a.u^3)	B (GPa)	B_P	E_{tot} (Ry)	E_c (eV per atom)
Rb_2YAuI_6	12.07	2966.75	21.96	2.63	−142 222.705247	1.40
Rb_2ScInI_6[24]	12.12		18.85			
Cs_2YAuI_6	12.11	3002.41	22.66	3.68	−161 457.950263	1.34
Cs_2ScInI_6[24]	12.15		17.95			

Table 2 Calculated values of the Bulk modulus (B), Shear modulus (G), Young's modulus (E), Poisson's ratio (σ), Pugh ratio (B/G), Cauchy pressure C^P, sound velocities (m s^{-1}), Debye temperature Θ_D (K) of A_2YAuI_6 (A = Rb, Cs) compared with the previous literature

Material property	Rb$_2$YAuI$_6$	Cs$_2$YAuI$_6$	Rb$_2$ScInI$_6$[24]	Cs$_2$ScInI$_6$[24]	Rb$_2$LiGaI$_6$[27]	Cs$_2$LiGaI$_6$[27]
Bulk modulus, B (GPa)	20.33	19.87	19.42	18.93	14.3699	18.6031
Shear modulus, G (GPa)	1.41	1.16	6.55	3.64		
t_G	0.954	0.995	0.95	0.97	0.9021	0.8152
Formation energy ΔH_f	−1.296	−1.335	−1.04	−1.16		
Young modulus, E (GPa)	4.15	3.43	17.67	10.24	18.8063	25.3824
Poisson ratio, σ (GPa)	0.47	0.47			0.245	0.232
Pugh ratio, B/G (GPa)	2.01	1.86	2.96	5.2	1.626	1.532
Cauchy pressure C^P (GPa)	18	17.9				
Transverse sound velocity (m s^{-1})	2092	1774				
Longitudinal sound velocity (m s^{-1})	3203	2874				
Average sound velocity (m s^{-1})	2293	1956				
Temperature Θ_D (K)	193.4	164.3	197.72	148.81		

4. Electronic properties

One of the most crucial electronic properties that aids in understanding a compound's device applications is its band gap, which offers a thorough explanation of its optical, electronic, and thermodynamic characteristics. We calculated the band structures of Rb$_2$YAuI$_6$ and Cs$_2$YAuI$_6$ by using PBE-GGA, TB-mBJ potential with and without spin orbit coupling (SOC) in order to analyze the electronic structure properties, as depicted in Fig. 3(a–f). The numerical values of the electronic band structure are presented in Table 3. Furthermore, as shown in Fig. 3(a–d), we identified substantially underestimated energy band gap values for the examined compounds utilizing the PBE-GGA technique. Based on this, the Tb-mBJ functional is a better exchange correlation functional for improving the optoelectronic features.[44] The energy band gap of 1.77 eV and 1.72 eV

has been observed for Rb$_2$YAuI$_6$ and Cs$_2$YAuI$_6$, respectively, by the Tb-mBJ potential. Applying SOC is essential in order to acquire the right bandgap values in relation to the values derived from experiments.[45] Consequently, we employed mBJ + SOC potentials to explore the Cs$_2$YAuI$_6$ (E_g = 1.73 eV) and Rb$_2$YAuI$_6$ (E_g = 1.70 eV) bandgap values. The band gap decreased as the atomic numbers of A (Rb, Cs) increased. The well-known inter-site exchange interactions can be connected to this. This has a direct relationship with the coinciding orbital overlaps, which scale inversely with the lattice constants.[46] Furthermore, the bands have been divided by the spin–orbit coupling (SOC). It was found that the SOC splitting inside the valence/conduction bands was stronger, and decreased the band gap width with bigger elemental components.

Total Density of States (TDOS) has been computed for the purpose of verifying the results of the energy band structure study. The Fermi level is shown by a vertical dashed line in all
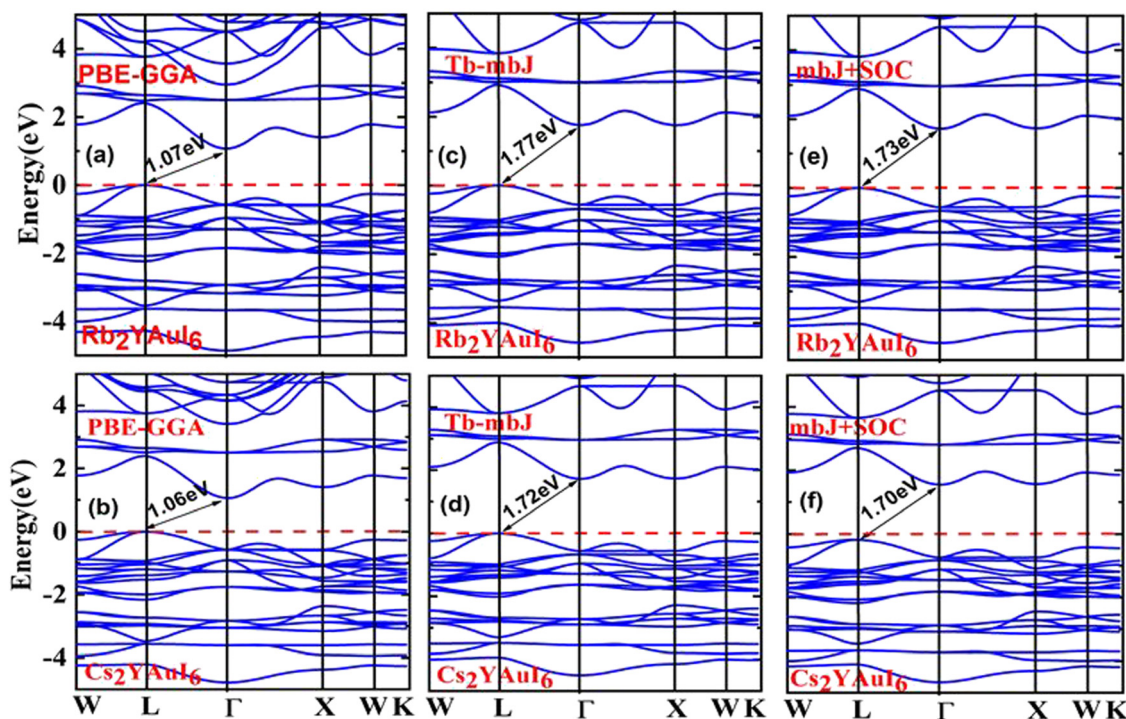

Fig. 3 Representations of the band structures of A_2YAuI_6 (A = Rb, Cs) using (a, b) PBE-GGA, (c, d) TB-mBJ and (e, f) mBJ + SOC approximation.

Table 3 Calculated energy bandgap (in eV) of A_2YAuI_6 (A = Rb, Cs) by different potentials, PBE, mBJ and mBJ + SOC

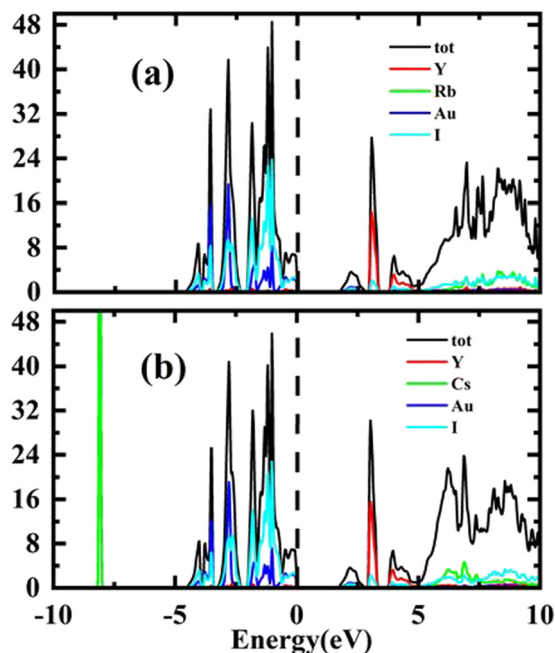| Properties	PBE	mBJ	mBJ + SOC
Rb_2YAuI_6	1.07	1.77	1.73
Cs_2YAuI_6	1.06	1.72	1.70

Fig. 4 Representations of the TDOS of (a) Rb_2YAuI_6, (b) Cs_2YAuI_6 using Tb-mBJ approximation.

partial density of states (PDOS) and total density of states (TDOS) graphs. The energy plots range from −10 eV to 10 eV. Conduction band (CB) states appear at positive energy, whereas the valence band (VB) states are present at negative energy. The total of the individual states is shown by TDOS in both conduction and valence bands resembling the band structure. The total density of states TDOS results are depicted in Fig. 4(a and b).

The results of PDOS for the studied compounds that describe the orbital contribution to the electron conduction mechanism are elaborated in Fig. 5(a and b). For Rb_2YAuI_6, the valence band formation is due to hybridization of the Au-5d and I-5p states. Meanwhile, the conduction band is occupied due to the hybridization of the Y-4d and Rb-5p states with a negligible contribution of the Au-5p states. In the case of Cs_2YAuI_6, the valence band is formed due to hybridization of electrons from I-5p and Au-5p and a nominal contribution of Cs-6s. However, the conduction band is occupied by hybridization of the Y-4d and Cs-4d states and a negligible contribution of the I-5p and Au-5p states.

4.1 The ELF and bader charge analysis

To investigate the nature of the bond identified between the constituents of the examined material, the electron localization function (ELF) is determined,[47] as illustrated in Fig. 6(a and b). The ELF is based on the probability density of locating an electron at a certain position in space, and offers information about how localized or delocalized the electrons are. There is no charge between the components of an ionic connection, in contrast to atoms in covalent and metallic bonds sharing a charge. Fig. 6 shows the spatial charge configuration for the Rb_2YAuI_6 and Cs_2YAuI_6 perovskites.

There are no charge contours that cross over to overlap with the I atoms in the perfectly spherical charge distribution between Rb and Y/Au. It was shown that there was an ionic connection between the I atom and the Cs, Rb atoms. In contrast, the Rb charge distribution varies from perfectly spherical to distorted, leading to a covalent interaction with the Cs atom (dumbbell type). It has been established that I accepts electrons from the Au network due to its covalent characteristics.

5. Optical properties

The optical properties were thoroughly explored in order to identify the importance of the computed material for solar cell applications. The optical performance of the transition study
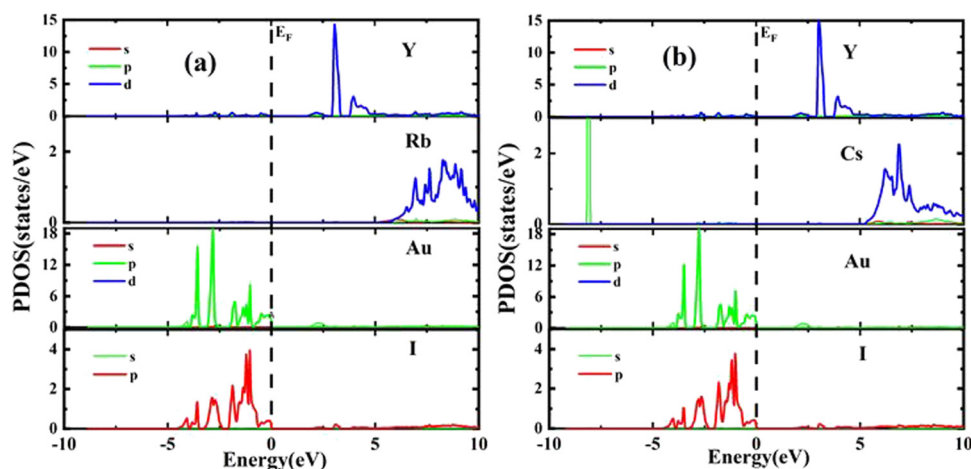

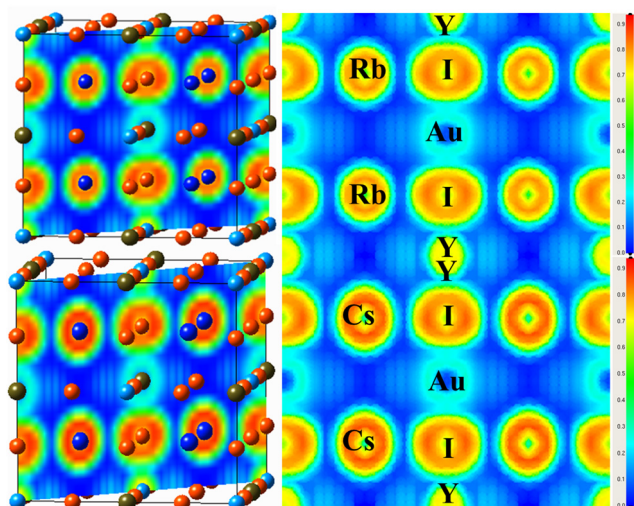**Fig. 5** Representations of the PDOS of (a) Rb_2YAuI_6, (b) Cs_2YAuI_6, using Tb-mBJ approximation.

Fig. 6 Representations of the ELF of A_2YAuI_6 (A = Rb, Cs) along the 101 plane direction using PBE-GGA approximation.

examined in relation to the optoelectronic features. The complex dielectric (CD) functions[48] are represented as follows:

$$\varepsilon(\omega) = \varepsilon_1(\omega) + i\varepsilon_2(\omega) \tag{5}$$

Fig. 7(a and b) displays the energy value 0–12 eV of the CD function plot. The dielectric constant has two parts: the imaginary part is denoted by $\varepsilon_2(\omega)$, and the real part represents $\varepsilon_1(\omega)$. The real and imaginary components of the dielectric function are related by the most familiar Kramers–Kronig equations,[49] which are given as:

$$\varepsilon_1(\omega) = 1 + \frac{2p}{\pi}\int_0^\infty \frac{\omega'\varepsilon_2(\omega')}{\left(\omega'^2 - \omega^2\right)}d\omega' \tag{6}$$

The imaginary portion is indicated as,

$$\varepsilon_2(\hbar\omega) = \frac{2\pi e^2}{\Omega\varepsilon_o}\sum |\psi_k^c|u.r|\psi_k^v|^2\delta\left(E_k^c - E_k^v - E\right) \tag{7}$$

Here, e indicates the electric charge, u is the electric field, and E_k^c, E_k^v and E stand for the energies of photons in the conduction band, valence band, and total photonic energy, respectively. The most significant portion of the $\varepsilon_1(\omega)$ spectrum is the 0 Hz limit $\varepsilon_1(0)$, which only specifies the dielectric function's electronic factor. The static dielectric function values of 4.06 and 4.11 have been observed for Rb_2YAuI_6 and Cs_2YAuI_6, respectively. The maximum peaks examined for Rb_2YAuI_6 and Cs_2YAuI_6 are 3.98 and 3.88 eV, respectively. It is important to note that the static dielectric function and electronic energy

from the valence to the conduction band was examined. The optical properties are illustrated by the relative positions of light and materials. The intensity of light emission and absorption for optoelectronic devices is determined by the inter- and intra-band transitions.

The complex dielectric function ($\varepsilon(\omega)$), absorption coefficient ($\alpha(\omega)$), complex refractive index ($n(\omega)$), reflectivity $R(\omega)$, loss function $L(\omega)$ and optical conductivity $\sigma(\omega)$ have all been
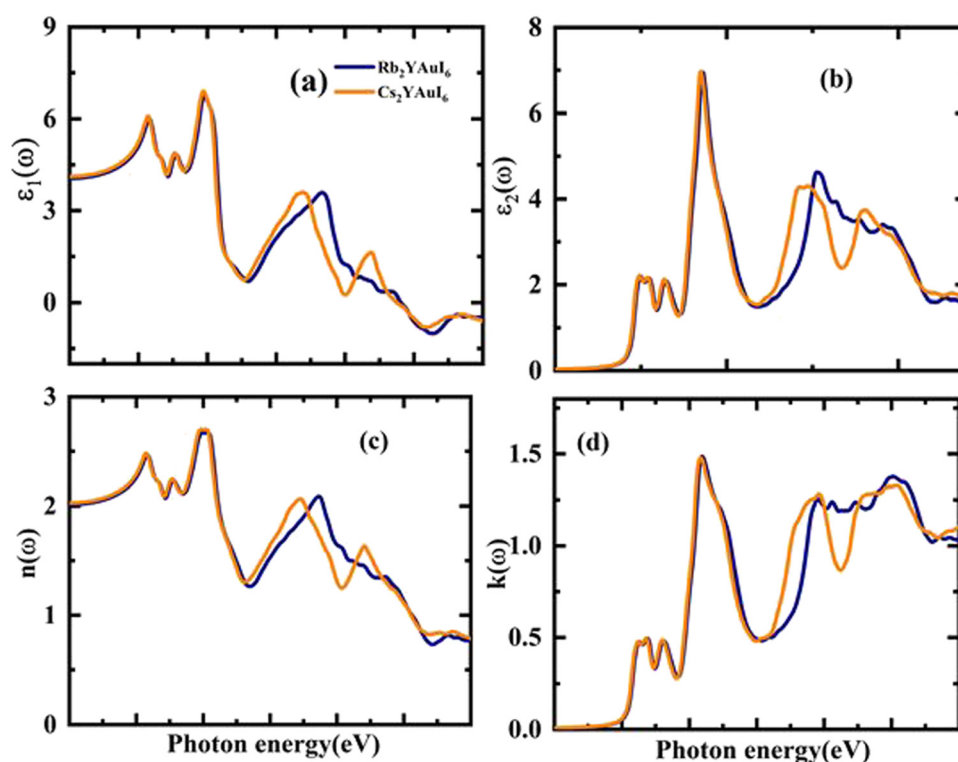

Fig. 7 The calculated energy-dependent optical parameters: (a) real part of the dielectric function, (b) imaginary part of the dielectric function, (c) refractive index coefficient, and (d) extinction coefficient of A_2YAuI_6 (A = Rb, Cs).

Table 4 Calculated optical properties of A_2YAuI_6 (A = Rb, Cs) by mBJ-GGA compared with literature

	Material property	Rb_2YAuI_6	Cs_2YAuI_6	Rb_2ScInI_6[24]	Cs_2ScInI_6[24]	Rb_2LiGaI_6[27]	Cs_2LiGaI_6[27]
Optical properties	$\varepsilon_1(0)$	4.06	4.11	21.12	17.82	3.3	3.45
	$n(0)$	2.01	2.03	4.59	4.22	1.83	1.85
	$R(0)$	0.113	0.115				

band gap are associated with each other, as shown in Table 4, according to the Pens model.[50]

Possible light-energy absorptions leading to an inter-band transition have been associated with $\varepsilon_2(\omega)$. This can be seen in Fig. 7(b), where the visible portions of the two computed compounds are the primary focus of the light absorptions. Cs_2YAuI_6 has a smaller bandgap that polarizes electron transfer in the conductance band and improves the photovoltaic outcomes. The methodical examination of $\varepsilon_1(\omega)$ and $\varepsilon_2(\omega)$ revealed that Rb_2YAuI_6 and Cs_2YAuI_6 have shown sufficient energy to absorb light in the broad range of wavelengths from 2–5 eV. Fig. 7(c and d) displays the complex refractive index. The real part of $n(\omega)$ in any medium of electromagnetic wave (EM) is the measurement of the phase velocity. Additionally, the imaginary component $k(\omega)$ arises as a result of an electromagnetic wave propagating through the same medium. The calculated static value $n(0)$ has been observed at 2.01 and 2.03 for Rb_2YAuI_6 and Cs_2YAuI_6, respectively. The imaginary $k(\omega)$ and real $n(\omega)$ components of the maximum estimated values for Rb_2YAuI_6 are observed at 2.47 eV and 2.64 eV, respectively. Upon converting the composition to Cs_2YAuI_6, these values changed to 1.48 eV

and 2.66 eV, respectively. When some halides are exposed to a specific frequency of photon radiation, the electrons begin to condense.

The electronic conduction causes this optical conductivity ($\sigma(\omega)$), which is depicted in Fig. 8(a). The first peak of $\sigma(\omega)$ has been observed for Rb_2YAuI_6 at 718 $(\omega\ cm)^{-1}$ at 2.54 eV, and the highest value of conductivity is found at 4772 $(\omega\ cm)^{-1}$ at 7.68 eV. On the other hand, the first peak of 721 at 2.21 eV with a maximum conductivity is 4533 at 9.12 eV for Cs_2YAuI_6.

The distance is measured prior to the absorption of light at a particular frequency. It is clear that the absorption coefficient spectrum $\alpha(\omega)$ for Rb_2YAuI_6 begins at 2.21 eV and peaks at 10.54 eV as s displaced in Fig. 8(b). However, for Cs_2YAuI_6, $\alpha(\omega)$ begins at 2.20 eV and reaches its maximum value at 10.20 eV. When the approaching photons reach the absorption edge, a dramatic increase in the absorption coefficient values is also noticed. Meanwhile, the optical absorptions of Cs_2LiGaI_6 and Rb_2LiGaI_6 have their initial maximum absorption bands and conductivity peaks in the visible energy band of (2.8–3.0 eV) and (2.65–2.8 eV), respectively.[27] It has been
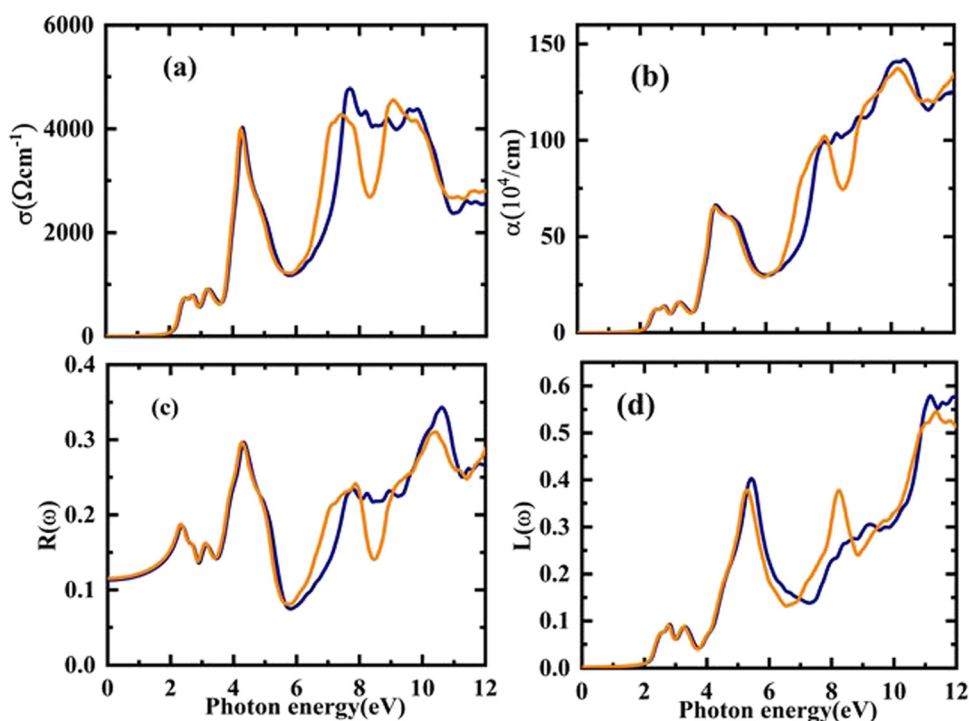

Fig. 8 The calculated energy-dependent optical parameters: (a) optical conductivity, (b) absorption coefficient, (c) optical reflectivity, and (d) energy loss function of A_2YAuI_6 (A = Rb, Cs).

Table 5 Calculated transport properties of A_2YAuI_6 (A = Rb, Cs) by mBJ-GGA

	Material property	Rb_2YAuI_6	Cs_2YAuI_6
Transport properties (300 K)	σ/τ (10^{18} Ω^{-1} m^{-1} s^{-1})	9.14	8.68
	S (μV K^{-1})	207	212
	R_H (10^{-8} m^3 C^{-1})	1.96	2.04
	κ_e (10^{14} W m^{-1} K^{-1} s^{-1})	1.57	1.53
	$S^2\sigma/\tau$ (10^{11} W K^{-2} m^{-1} s^{-1})	3.93	3.89

observed that our examined compounds can absorb electromagnetic radiation from the (UV-visible) region with wavelengths of 119–562 nm for Rb_2YAuI_6 and 122–565 nm for Cs_2YAuI_6, as shown in Fig. 8(b). This further supports the validity of these materials in the solar energy industry. The results of the optical absorption show that both compounds can absorb a wide UV-visible range of electromagnetic radiation in accordance with their electronic behavior, making it a potential candidate for optoelectronic and solar cell applications.

Similar to the previous discussion of optical parameters, the reflectivity $R(\omega)$ and optical loss $L(\omega)$ are significant variables, and their values should be low for the best optical materials. The surface morphology of the studied compounds is depicted by $R(\omega)$. The computed $R(\omega)$ values are displayed in Fig. 8(c). For Rb_2YAuI_6 and Cs_2YAuI_6, their values at zero energy are 0.113 and 0.115, respectively. The maximum value of reflectivity has been observed at 10.62 eV (0.34) and 10.38 eV. The light scattering and dispersion are displaced in Fig. 8(d), as illustrated by $L(\omega)$. It is worth mentioning that minimal energy loss has been observed in the visible region, which shows that these materials are suitable for solar cell applications.

6. Thermoelectric properties

Based on the figure of merit (ZT) provided by $ZT = \left(S^2 \dfrac{\sigma T}{K} \right)$,[51–53] we have evaluated the thermoelectric efficiency of our examined compounds. The enhanced Seebeck coefficient (S), higher electrical conductivity (σ), and lowered thermal conductivity (κ) describe an effective thermoelectric compound. For Rb_2YAuI_6 and Cs_2YAuI_6, we have calculated their thermoelectric properties in relation to the temperature T (K), chemical potential μ (eV) and carrier concentration N (e/u.c) using the Boltztrap code.[36] All calculated transport parameters at room temperature, *i.e.*, 300 K, are tabulated in Table 5.

The carrier's concentration has been used to classify the p and n-type features. The energy required to add or remove electrons from the material is indicated by μ. When electrons are introduced into the system, μ is positive. When they are taken out of the system, the μ is negative. The system operates as an n-type material when electrons are introduced. When electrons are removed, the system becomes more hole-filled, indicating that the materials under study are p-type.[54] Additionally, Fig. 4 shows that the DOS are more heavily occupied in the valence band than in the conduction band, confirming the p-type character of holes and their function as dominating charge carriers. The possibility that carriers will exist is represented by the density of states. Compared to the conduction band, the valence band contains a higher density of closely spaced states, indicating that there are more carriers available there. In semiconductors, the behavior becomes p-type if there are more holes (VB) than electrons (CB).

The Seebeck coefficient (S) may be expressed as $S = \Delta V/\Delta T$, where ΔT denotes the temperature gradient. The Seebeck coefficient is the material's capacity to produce induced emf
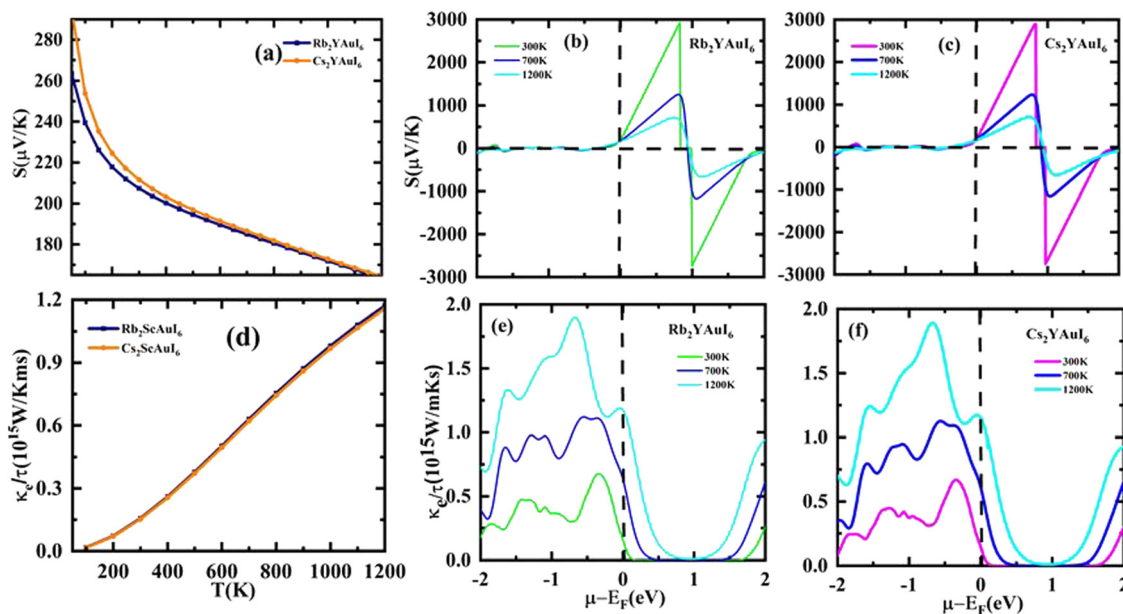

Fig. 9 Variation of the band structures of A_2YAuI_6 (A = Rb, Cs) with temperature using TB-mBJ approximation: (a) Seebeck coefficients, (b) and (c) Seebeck coefficients against chemical potential, (d) electrical conductivity, (e) and (f) electrical conductivity *versus* chemical potential.
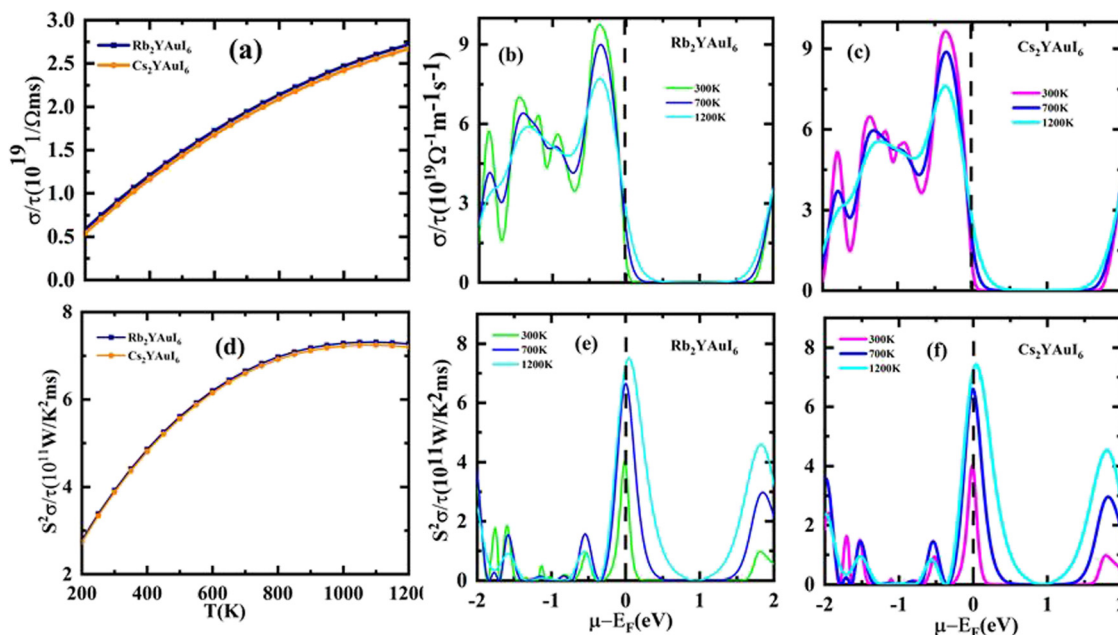
Fig. 10 Variation of the band structures of A_2YAuI_6 (A = Rb, Cs) with temperature using TB-mBJ approximation: (a) electronic thermal conductivity, (b) and (c) electronic thermal conductivity against chemical potential, (d) power factor, (e) and (f) power factor *versus* chemical potential.

when a temperature differential is applied. Fig. 9(a) displays the computation of the Seebeck coefficient (S) alongside T. As the temperature rises, the value of S decreases. For two complexes, the value of S is positive, indicating that the majority of the
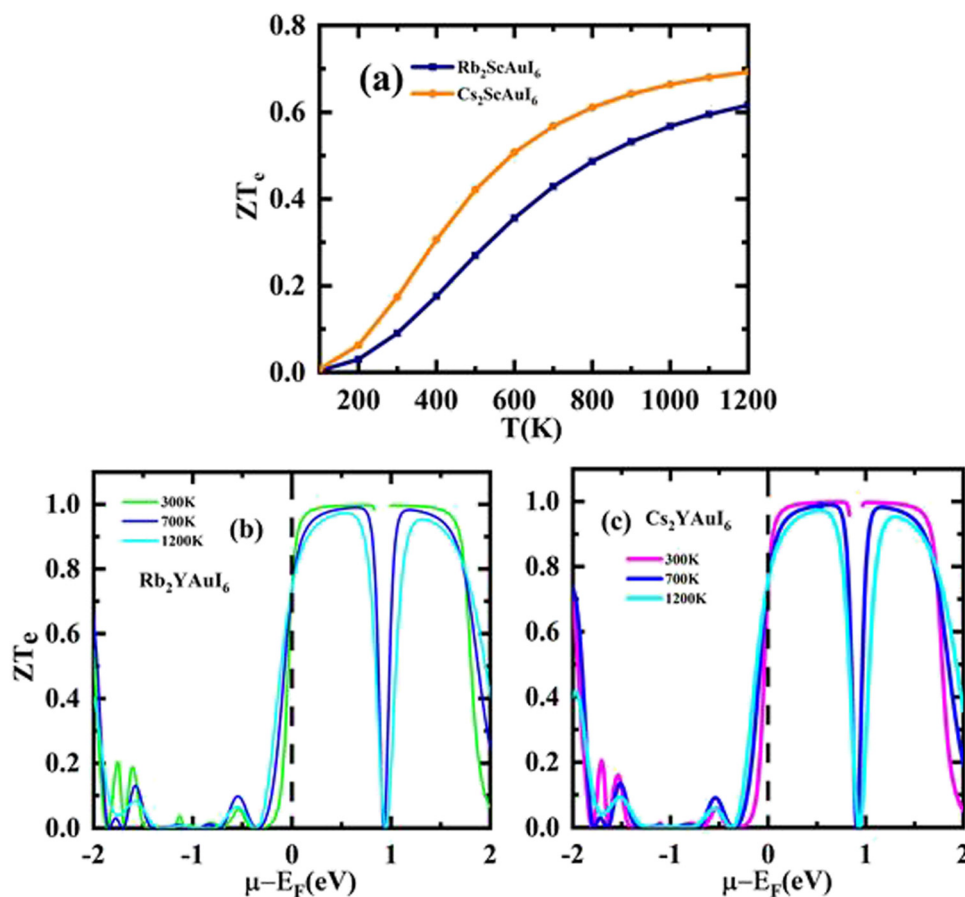

Fig. 11 The computed results of figure of merit by Tb-mBJ (a) ZT against temperature, (b) and (c) ZT versus chemical potential.

charge carriers in those materials are holes. The calculated values of S at room temperature are 207.3 μV K^{-1} (Rb$_2$YAuI$_6$) and 211.6 μV K^{-1} (Cs$_2$YAuI$_6$). Fig. 9(b) shows the Seebeck coefficient for the given material at different Kelvin temperatures *versus* chemical potential. It is clear that the Seebeck coefficient shows distinct peaks and slopes over the whole chemical potential range.

The chemical potential of the p-type region has the highest value, 2925 μV K^{-1} for (Rb$_2$YAuI$_6$) and 2897 μV K^{-1} for (Cs$_2$YAuI$_6$) at room temperature. The chemical in consideration exhibits a greater Seebeck coefficient value due to its large band gap and restricted carrier mobility. However, at higher temperatures, S is somewhat dropped to 719 μV K^{-1} and 708 μV K^{-1} for Rb$_2$YAuI$_6$ and Cs$_2$YAuI$_6$, respectively. The bipolar effect, which continues when bound electrons are propelled by thermal energy and create electron–hole pairs, is responsible for the drop in the Seebeck coefficient at higher temperatures. These findings entirely agree with the Mott relationship, which measures how much temperature and chemical potential influence the Seebeck coefficient.[55] The current material may find application in temperature sensors, thermocouples, thermoelectric coolers, and generators due to its non-zero value of S at high temperatures.

The material flow is caused by electronic movement (k_{el}) and lattice vibration (k_{ph}), which also results in thermal conductivity (k_e/τ).[56] Electrons are triggered by elastic waves produced by lattice vibration. Therefore, when estimating the electronic component of k_e/τ, we ignored the phononic element of the thermal conductivity. Fig. 9(c) shows the thermal conductivity against the chemical potential, while Fig. 9(d) shows the behavior of the thermal conductivity against temperature. The k_e/τ rises as the temperature rises because a higher temperature increases the carrier mobility, which in turn improves the electronic movement and raises the electronic thermal conductivity.

The electrical conductivity (σ/τ) *versus* chemical potential m (eV) is represented in Fig. 10(b and c), whereas the electrical conductivity *versus* temperature (K) is shown in Fig. 10(a). The chemical potential, whose value is 0 at the Fermi level, is the necessary amount of energy to get the electrons included in the circuit for overcoming the Coulomb potential. The chemical potential could either have a positive or negative value. The p-type behavior is expressed by the negative value, and the n-type reaction is represented by the positive value.[57,58] A greater number of conduction electrons are present at high energies, as indicated by the high values of σ/τ between 0 and -0.7 and -0.8 eV for Rb$_2$YAuI$_6$ and Cs$_2$YAuI$_6$, respectively. The σ/τ peak for Rb$_2$YAuI$_6$ indicates a large intensity (which means it includes more conduction electrons than Cs$_2$YAuI$_6$), which is in accordance to previous studies.[24]

The power factor ($S^2\sigma/\tau$) computed to guess the thermoelectric strength of the examined compounds *versus* temperature and chemical potential is displayed in Fig. 10(a and b). As the temperature rises, the power factor increases linearly, as demonstrated by the sharp decline in the value of the Seebeck coefficient depicted in Fig. 9(a).
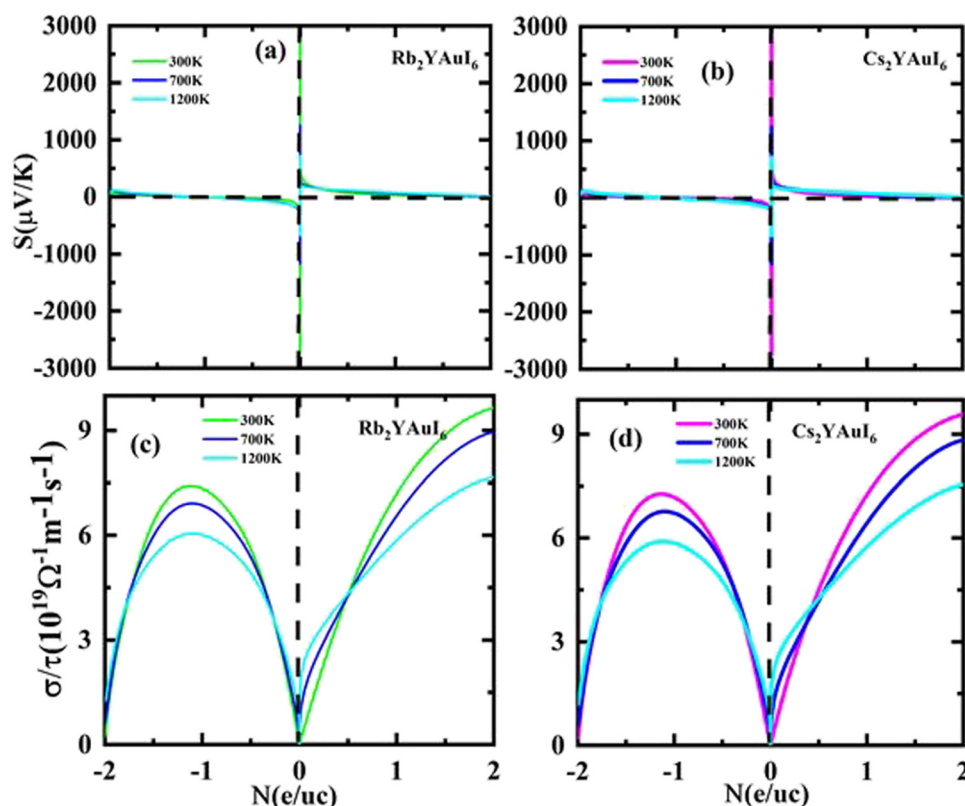

Fig. 12 Accomplished thermoelectric properties (a, b) S and (c, d) σ/τ against the carrier concentration of A$_2$YAuI$_6$ (A = Rb, Cs) using the TB-mBJ approximation.
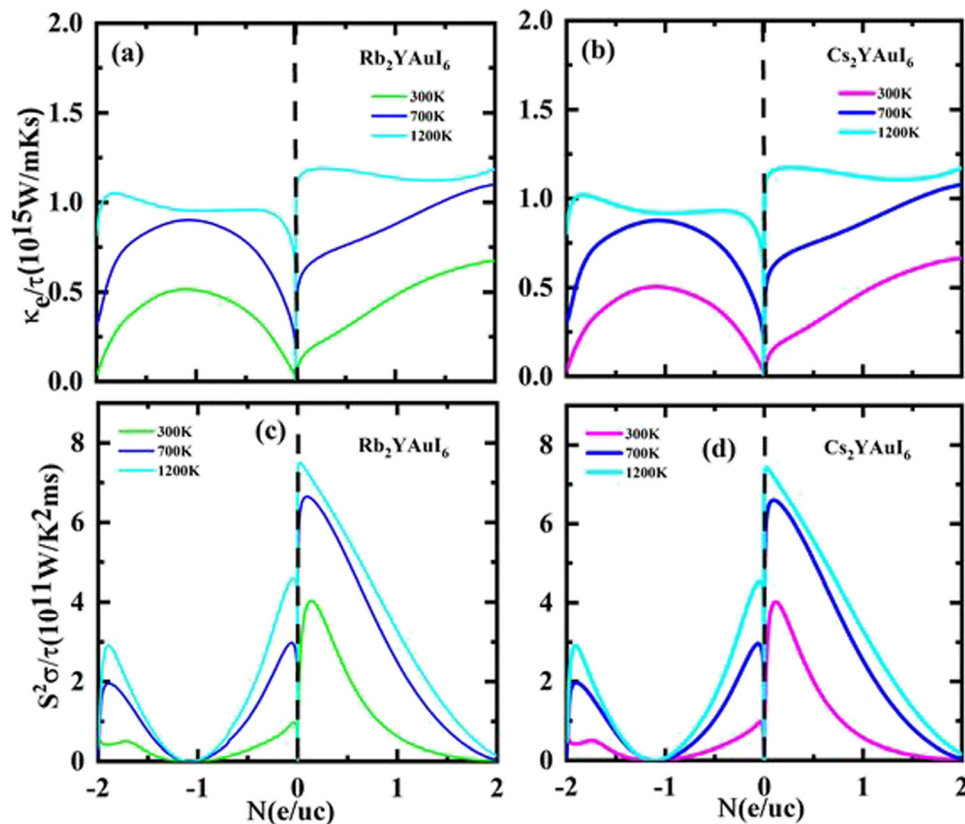
Fig. 13 Accomplished thermoelectric properties (a, b) $\kappa e/\tau$ and (c, d) PF against the carrier concentration of A_2YAuI_6 (A = Rb, Cs) using the TB-mBJ approximation.

A factor known as the figure of merit is in charge of the compound thermoelectric activity. Furthermore, by dividing the power factor by thermal conductivity, this factor is used to calculate the true thermoelectric efficiency.[51] ZT alongside temperature (T) is displayed in Fig. 11(a), and also against the chemical potential, as shown in Fig. 11(b and c) respectively. The maximum value of ZT is 0.98 at the chemical potential value of 0.48 eV for Rb_2YAuI_6 and 0.99 at 0.50 eV for Cs_2YAuI_6 at room temperature, 300 K. In other studies, the value of ZT decreased

with the rise in temperature.[24] As a result, the compounds under study exhibit a high ZT at room temperature. The description above makes clear how crucial the analysis is for thermoelectric generators and other thermoelectric functions.

The Seebeck coefficients S and σ/τ *versus* N (e/u.c) with positive and negative doping in the materials are shown in Fig. 12(a–d). Increasing the doping and temperature (K) and σ/τ do not alter the graphs of the Seebeck coefficient. Thus, as illustrated in Fig. 12(a and b), we found that the Cs_2YAuI_6

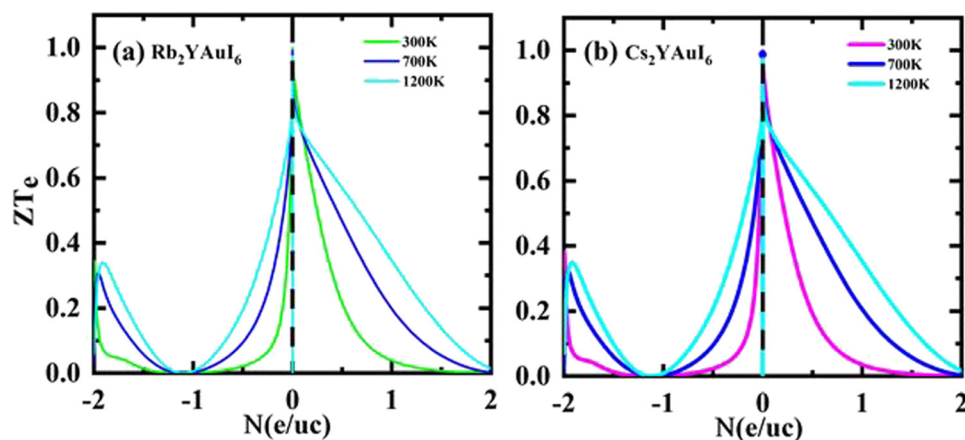**Fig. 14** Calculated thermoelectric properties figure of merit ZT against the carrier concentration of (a) Rb_2YAuI_6, (b) Cs_2YAuI_6 using TB-mBJ approximation.

molecule exhibits a significant variance in p-type doping from 0 to 0.2. Furthermore, for both compounds under study, a maximum accomplishment in σ/τ is observed at 1.1 N (e/u.c). The electronic thermal conductivity (k_e/τ) of the explored composites has been calculated in order to investigate the heat energy created by the materials. We investigated these materials against n-type and p-type doping at temperatures of 300, 700, and 1200 K. The electronic conductivity is presented in Fig. 13(a and b) against the carrier concentration. For the Rb_2YAuI_6 compound, we managed to achieve the maximum value at 300, 700, and 1200 K, which is 0.51×10^{15} W m^{-1} K^{-1} s^{-1}, 0.90×10^{15} W m^{-1} K^{-1} s^{-1} at -1.1 N (e/u.c) and 1.05×10^{15} at -1.86 N (e/u.c). Similarly, Cs_2YAuI_6 has values at 300, 700, and 1200 with 0.50×10^{15} W m^{-1} K^{-1} s^{-1}, 0.87×10^{15} W m^{-1} K^{-1} s^{-1} at -1.1 N (e/u.c), and 1.02×10^{15} at -1.86 N (e/u.c).

The PF for both double perovskites is shown in Fig. 13(c and d) at various temperatures, including 300, 700, and 1200 K at 1 N (e/u.c). For n-type doping, there is no PF, but both materials achieve values close to the Fermi level at 1200 K, which is 7.44×10^{11} and 7.40×10^{11} W m^{-1} K^{-2} s^{-1} for Rb_2YAuI_6 and Cs_2YAuI_6, respectively.

Fig. 14(a and b) shows that for both compounds under study, the ZT values at 0 N (e/u.c) are 1, but that the ZT values sharply decline with increasing p-type doping and linearly decrease with increasing n-type doping.

7. Conclusion

In our study, we computed the opto-electronic and thermo-electric features of A_2YAuI_6 (A = Rb, Cs) using DFT calculations. The PBE generalized gradient approximation has been implemented to optimize the structural parameters. In order to acquire appropriate energy band gaps, Tb-mBJ with and without SOC schemes were used instead of PBE-GGA. It has been established that Rb_2YAuI_6 is more ductile than Cs_2YAuI_6 due to its higher Pugh's and Poisson's ratio values. The materials have indirect bandgaps of 1.73 and 1.70 eV for Rb_2YAuI_6 and Cs_2YAuI_6, respectively, which are potential materials for the manufacturing of solar cell devices and lie in the UV-visible region of the EM spectrum. The negative values of the formation energy and tolerance factor show that the examined materials are thermodynamically stable. The ELF plots demonstrate that there is an ionic connection between Rb/CS, I, and Au. The solar cells are favored by the lowest values of optical loss and reflection, combined with significant visible light attenuation. Thermoelectric generator applications benefit greatly from the huge values of ZT, Seebeck coefficient, and PF at low temperatures of 300 K, as well as the ultralow value of the lattice vibration. As a result, these compounds will provide the experimental community with profound insight into how to implement them to advance the solar cell and thermoelectric generator industries.

Conflicts of interest

There are no conflicts to declare.

Acknowledgements

References

1 J. Chen, X. Cai, D. Yang, D. Song, J. Wang and J. Jiang, *et al.*, Recent progress in stabilizing hybrid perovskites for solar cell applications, *J. Power Sources*, 2017, **355**, 98–133.

2 M. J. Fang, C. W. Tsao and Y. J. Hsu, Semiconductor nano-hetero structures for photo-conversion applications, *J. Phys. D: Appl. Phys.*, 2020, **53**, 143001.

3 S. Choudhary, A. Shukla, J. Chaudhary and A. S. Verma, Extensive investigation of structural, electronic, optical, and thermoelectric properties of hybrid perovskite ($CH_3NH_3PbBr_3$) with mechanical stability constants, *Int. J. Energy Res.*, 2020, **44**, 11614–11628.

4 Y. Saeed, B. Amin, H. Khalil, F. Rehman, H. Ali and M. I. Khan, *et al.*, $Cs_2NaGaBr_6$: a new lead-free and direct band gap halide double perovskite, *RSC Adv.*, 2020, **10**, 17444–17451.

5 Y. Jia, Y. Zeng, X. Li and L. Meng, Effect of Sr substitution on the property and stability of $CH_3NH_3SnI_3$ perovskite: a first principles investigation, *Int. J. Energy Res.*, 2020, **44**, 5765–5778.

6 R. Kour, S. Arya, S. Verma, J. Gupta, P. Bandhoria and V. Bharti, *et al.*, Potential substitutes for replacement of lead in perovskite solar cells: a review, *Global Challenge*, 2019, **3**, 1900050.

7 D. Zhou, T. Zhou, Y. Tian, X. Zhu and Y. Tu, Perovskite-based solar cells: materials, methods, and future perspectives, *J. Nanomater.*, 2018, **2018**, 8148072.

8 M. Palummo, E. Berrios, D. Varsano and G. Giorgi, Optical properties of lead-free double perovskites by ab initio excited-state methods, *ACS Energy Lett.*, 2020, **5**, 457–463.

9 G. Volonakis, A. A. Haghighirad, R. L. Milot, W. H. Sio, M. R. Filip and B. Wenger, *et al.*, Cs_2InAgC_{16}: a new lead-free halide double perovskite with direct band gap, *J. Phys. Chem. Lett.*, 2017, **8**, 772–778.

10 B. K. Ghosh and T. K. Biswas, Emerging solar cells energy trade-off: interface engineering materials impact on stability and efficiency progress, *Int. J. Energy Res.*, 2019, **43**, 1670–1688.

11 C. Shi, J. J. Ma, J. Y. Jiang, M. M. Hua, Q. Xu and H. Yu, *et al.*, Large piezoelectric response in hybrid rare-earth double perovskite relaxor ferroelectrics, *J. Am. Chem. Soc.*, 2020, **142**, 9634–9641.

12 C. C. Stoumpos, C. D. Malliakas and M. G. Kanatzidis, Semiconducting tin and lead iodide perovskites with organic cations: phase transitions, high mobilities, and near-infrared photoluminescent properties, *Inorg. Chem.*, 2013, **52**, 9019–9038.

13 N. K. Noel, S. D. Stranks, A. Abate, C. Wehrenfennig, S. Guarnera and A. A. Haghighirad, *et al.*, Lead-free

organiceinorganic tin halide perovskites for photovoltaic applications, *Energy Environ. Sci.*, 2014, **7**, 3061–3068.

14 F. Hao, C. C. Stoumpos, D. H. Cao, P. R. Chang and M. G. Kanatzidis, Lead-free solid-state organiceinorganic halide perovskite solar cells, *Nat. Photonics*, 2014, **8**, 489–494.

15 C. C. Stoumpos, C. D. Malliakas, J. A. Peters, Z. Liu, M. Sebastian and J. Im, *et al.*, Crystal growth of the perovskite semiconductor CsPbBr$_3$: a new material for high-energy radiation detection, *Cryst. Growth Des.*, 2013, **13**, 2722–2727.

16 M. Kulbak, D. Cahen and G. Hodes, How important is the organic part of lead halide perovskite photovoltaic cells? Efficient CsPbBr$_3$ cells, *J. Phys. Chem. Lett.*, 2015, **6**, 2452–2456.

17 M. Kulbak, S. Gupta, N. Kedem, I. Levine, T. Bendikov and G. Hodes, *et al.*, Cesium enhances long-term stability of lead bromide perovskite-based solar cells, *J. Phys. Chem. Lett.*, 2016, **7**, 167–172.

18 E. T. McClure, M. R. Ball, W. Windl and P. M. Woodward, Cs2AgBiX6 (X$\frac{1}{4}$ Br, Cl): new visible light absorbing, lead-free halide perovskite semiconductors, *Chem. Mater.*, 2016, **28**, 1348–1354.

19 T. Wang, D. Yue, X. Li and Y. Zhao, Lead-free double perovskite Cs$_2$AgBiBr$_6$/RGO composite for efficient visible light photo catalytic H$_2$ evolution, *Appl. Catal., B*, 2020, **268**, 118399.

20 S. R. Bhandari, D. K. Yadav, B. P. Belbase, M. Zeeshan, B. Sadhukhan and D. P. Rai, *et al.*, Electronic, magnetic, optical and thermoelectric properties of Ca$_2$Cr$_{1x}$ Ni$_x$OsO$_6$ double perovskites, *RSC Adv.*, 2020, **10**, 16179–16186.

21 C. C. Sorrell, S. Sugihara and J. Nowotny, *Materials for energy conversion devices*, Woodhead Pub. Limited, 2005, vol. 416.

22 E. Haque and M. A. Hossain, Electronic, phonon transport and thermoelectric properties of Cs$_2$InAgC$_{l6}$ from first-principles study, *Comput. Condensed Matter*, 2019, **19**, 00374.

23 M. Aslam Khan, H. A. Alburaih, N. A. Noor and A. Dahshan, Comprehensive investigation of Opto-electronic and transport properties of Cs$_2$ScAgX$_6$ (X$\frac{1}{4}$ Cl, Br, I) for solar cells and thermoelectric applications, *Sol. Energy*, 2021, **225**, 122–128.

24 N. A. Noor, M. W. Iqbal, T. Zelai, A. Mahmood, H. M. Shaikh, S. M. Ramay and W. Al Masry, Analysis of direct band gap A2ScInI6 (A$\frac{1}{4}$ Rb, Cs) double perovskite halides using DFT approach for renewable energy devices, *J. Mater. Res. Technol.*, 2021, **13**, 2491–2500.

25 S. Iqbal, G. M. Mustafa, M. Asghar, N. A. Noor, M. W. Iqbal, A. Mahmood and Y. H. Shin, Tuning the optoelectronic and thermoelectric characteristics of narrow bandgap Rb$_2$AlInX$_6$ (X$\frac{1}{4}$ Cl, Br, I) double perovskites: a DFT study, *Mater. Sci. Semicond. Process.*, 2022, **143**, 106551.

26 R. Anbarasan, M. Srinivasan, R. Suriakarthick, H. Albalawi, J. K. Sundar, P. Ramasamy and Q. Mahmood, Exploring the structural, mechanical, electronic, and optical properties of double perovskites of Cs$_2$AgInX$_6$ (X $\frac{1}{4}$ Cl, Br, I) by first principles calculations, *J. Solid State Chem.*, 2022, **310**, 123025.

27 S. Nazir, N. A. Noor, M. Manzoor and A. Dahshan, Ab-initio simulations of Li-based Double Perovksites A$_2$LiInBr$_6$ (A $\frac{1}{4}$ Rb, Cs) for solar cell applications, *Chem. Phys. Lett.*, 2022, **798**, 139612.

28 P. Blaha, K. Schwarz, G. K. H. Madsen, D. Kvasnicka and J. Luitz, *Techn. An Augmented Plane Wave+ Local Orbitals Program for Calculating Crystal Properties*, 2001.

29 K. Schwarz, P. Blaha and G. K. H. Madsen, Electronic structure calculations of solids using the WIEN2k package for material sciences, *Comput. Phys. Commun.*, 2002, **147**, 71.

30 M. Petersen, F. Wagner, L. Hufnagel, M. Scheffler, P. Blaha and K. Schwarz, Improving the efficiency of FP-LAPW calculations, *Comput. Phys. Commun.*, 2000, **126**, 294–309.

31 J. P. Perdew, A. Ruzsinszky, G. I. Csonka, O. A. Vydrov, G. E. Scuseria, L. A. Constantin, X. Zhou and K. Burke, Restoring the density-gradient expansion for exchange in solids and surfaces, *Phys. Rev. Lett.*, 2008, **100**, 136406.

32 J. P. Perdew, K. Burke and M. Ernzerhof, Generalized gradient approximation made simple, *Phys. Rev. Lett.*, 1996, **77**, 3865.

33 F. Tran and P. Blaha, Accurate band gaps of semiconductors and insulators with a semilocal exchange–correlation potential, *Phys. Rev. Lett.*, 2009, **102**, 226401.

34 J. P. Perdew, K. Burke and M. Ernzerhof, Generalized gradient approximation made simple, *Phys. Rev. Lett.*, 1996, **77**, 3865–3868.

35 P. E. Blöchl, O. Jepsen and O. K. Andersen, Improved tetrahedron method for Brillouin-zone integrations, *Phys. Rev. B: Condens. Matter Mater. Phys.*, 1994, **49**, 16223.

36 G. K. Madsen and D. J. Singh, BoltzTraP. A code for calculating band structure dependent quantities, *Comput. Phys. Commun.*, 2006, **175**, 67–71.

37 F. Birch, Finite elastic strain of cubic crystals, *Phys. Rev.*, 1947, **71**(11), 809.

38 Alexander E. Fedorovskiy, A. Drigo Nikita and Mohammad KhajaNazeeruddin, The role of Goldschmidt's tolerance factor in the formation of A2BX6 double halide perovskites and its optimal range, *Small Methods*, 2020, **4**(5), 1900426.

39 Q. Mahmood, T. Ghrib, A. Rached, A. Laref and M. A. Kamran, Probing of mechanical, optical and thermoelectric characteristics of double perovskites Cs$_2$GeCl/Br$_6$ by DFT method, *Mater. Sci. Semicond. Process.*, 2020, **112**, 105009.

40 M. Roknuzzaman, K. K. Ostrikov, H. Wang, A. Du and T. Tesfamichael, Towards lead-free perovskite photovoltaics and optoelectronics by ab-initio simulations, *Sci. Rep.*, 2017, **7**, 14025.

41 Y. O. Ciftci, K. Colakoglu, E. Deligoz and H. Ozisik, The first principles study on the LaN, *Mater. Chem. Phys.*, 2008, **108**, 120–123.

42 Y. J. Hao, X. R. Chen, H. L. Cui and Y. L. Bai, First-principles calculations of elastic constants of c-BN, *Phys. B*, 2006, **382**, 118–122.

43 M. Marathe, A. Grüneböhm, T. Nishimatsu, P. Entel and C. Ederer, First-principles-based calculation of the

electrocaloric effect in $BaTiO_3$: a comparison of direct and indirect methods, *Phys. Rev. B*, 2016, **93**, 054110.

44 E. A. Khera, U. Rasheed, M. Imran, H. Ullah, F. Hussain, R. A. Khalil and M. Qasim, An insight into structural, electronic and optical characteristics of $Mo_{1-x}M_xO_3$ (M= Zr, Y, ZrY) for the formation of conducting filaments in optoelectronic memory devices: A first principles study, *Optik*, 2022, **258**, 168913.

45 Y. Saeed, B. Amin, H. Khalil, F. Rehman, H. Ali and M. I. Khan, *et al.*, Correction: $Cs_2NaGaBr_6$: a new lead-free and direct band gap halide double perovskite, *RSC Adv.*, 2020, **10**, 20196.

46 R. Ahmed, N. S. Masuri, B. U. Haq, A. Shaari, S. AlFaifi, F. K. Butt and S. A. Tahir, Investigations of electronic and thermoelectric properties of half-Heusler alloys XMgN (X= Li, Na, K) by first-principles calculations, *Mater. Des.*, 2017, **136**, 196–203.

47 E. A. Khera, U. Rasheed, M. Imran, H. Ullah, F. Hussain, R. A. Khalil and M. Qasim, An insight into structural, electronic and optical characteristics of $Mo_{1-x}M_xO_3$ (M= Zr, Y, ZrY) for the formation of conducting filaments in optoelectronic memory devices: A first principles study, *Optik*, 2022, **258**, 168913.

48 M. H. Samat, A. M. M. Ali, M. F. M. Taib, O. H. Hassan and M. Z. A. Yahya, Hubbard U calculations on optical properties of 3d transition metal oxide TiO_2, *Results Phys.*, 2016, **6**, 891–896.

49 P. Puschnig and C. Ambrosch-Draxl, *Phys. Rev. B*, 2020, **66**, 165105.

50 D. R. Penn, Wave-number-dependent dielectric function of semiconductors, *Phys. Rev.*, 1962, **128**, 2093.

51 H. C. Wang, P. Pistor, M. A. L. Marques and S. Botti, Double perovskites as p-type conducting transparent semiconductors: a high-throughput search, *J. Mater. Chem.*, 2019, **7**, 14705.

52 Q. Mahmood, T. Zelai, T. Usman, S. Al-Qaisi, M. Morsi, H. Albalawi, A. I. Aljameel, O. A. Alamri and G. Murtaza, First-principles study of lead-free double perovskites $K_2Pt(Cl/Br)_6$ for optoelectronic and renewable energy applications, *J. Solid State Chem.*, 2021, **301**, 122294.

53 T. H. Flemban, V. Singaravelu, A. A. S. Devi and I. S. Roqan, Homogeneous vertical ZnOnanorod arrays with high conductivity on an in situ Gd nanolayer, *RSC Adv.*, 2015, **5**(115), 94670–94678.

54 Q. Mahmood, M. H. Alhossainy, M. S. Rashid, T. H. Flemban, H. Althib, T. Alshahrani, M. Rashid and A. Laref, First-principles study of lead-free double perovskites Rb_2TeX_6 (X $\frac{1}{4}$Cl, Br, and I) for solar cells and renewable energy, *Mater. Sci. Eng. B*, 2021, **266**, 115064.

55 M. Jonson and G. D. Mahan, *Phys. Rev. B: Condens. Matter Mater. Phys.*, 1980, **21**, 4223–4229.

56 J. P. Heremans, V. Jovovic, E. S. Toberer, A. Saramat, K. Kurosaki and A. Charoenphakdee, *et al.*, Enhancement of thermoelectric efficiency in PbTe by distortion of the electronic density of states, *Science*, 2008, **321**, 554–557.

57 M. Bilal, M. Shafiq, B. Khan, H. R. Aliabad, S. J. Asadabadi and R. Ahmad, *et al.*, Antiperovskite compounds $SbNSr_3$ and $BiNSr_3$: potential candidates for thermoelectric renewable energy generators, *Phys. Lett.*, 2015, **379**, 206–210.

58 F. Kim, B. Kwon, Y. Eom, J. E. Lee, S. Park and S. Jo, *et al.*, 3D printing of shape-conformable thermoelectric materials using all inorganic Bi_2Te_3-based inks, *Nat. Energy*, 2018, **3**, 301–309.